

Synchrotron based planar imaging and digital Tomosynthesis of breast and biopsy phantoms using a CMOS Active Pixel Sensor

Magdalena B. Szafraniec¹, Anastasios C. Konstantinidis¹, Giuliana Tromba², Diego Dreossi², Sara Vecchio³, Luigi Rigon², Nicola Sodini², Steve Naday⁴, Spencer Gunn⁴, Alan McArthur⁴ and Alessandro Olivo¹

¹Department of Medical Physics and Bioengineering, UCL, London WC1E 6BT, UK

²Sincrotrone Trieste, Basovizza, Trieste, Italy

³I.M.S. Internazionale Medico Scientifica, Bologna, Italy

⁴Dexela Ltd (a PerkinElmer company), London N17EU, UK

ABSTRACT

The SYRMEP (SYnchrotron Radiation for MEDical Physics) beamline at Elettra is performing the first mammography study on human patients using free-space propagation phase contrast imaging. The stricter spatial resolution requirements of this method currently force the use of conventional films or specialized computed radiography (CR) systems. This also prevents the implementation of three-dimensional (3D) approaches. This paper explores the use of an X-ray detector based on complementary metal-oxide-semiconductor (CMOS) active pixel sensor (APS) technology as a possible alternative, for acquisitions both in planar and tomosynthesis geometry.

Results indicate higher quality of the images acquired with the synchrotron set-up in both geometries. This improvement can be partly ascribed to the use of parallel, collimated and monochromatic synchrotron radiation (resulting in scatter rejection, no penumbra-induced blurring and optimized X-ray energy), and partly to phase contrast effects. Even though the pixel size of the used detector is still too large – and thus suboptimal – for free-space propagation phase contrast imaging, a degree of phase-induced edge enhancement can clearly be observed in the images.

Corresponding author: Magdalena Szafraniec, m.szafraniec@ucl.ac.uk, University College London, Mullard Space Science Laboratory, Holmbury Hill Road, Dorking, Surrey RH5 6NT, UK

Keywords: Phase Contrast Imaging, Tomosynthesis, Flat Panel Detector, CMOS, APS, Mammography, Edge Enhancement, Image Contrast, 3D Breast Imaging

I. INTRODUCTION

Digital X-ray detectors based on complementary metal-oxide-semiconductor (CMOS) active pixel sensor (APS) technology have been recently introduced in mammographic imaging, especially in relatively new fields such as digital breast tomosynthesis (DBT) [1, 2]. Considering the difficulties involved in a full three-dimensional (3D) computed tomography (CT) acquisition of the female breast, partial view tomography performed in tomosynthesis conditions offers a valuable alternative. Although full tomographic slices are not reconstructed, DBT allows “slicing” the sample volume in separate layers along the main x-ray propagation direction, thus solving to a good extent the “structural noise” problem caused by overlying structures [3]. At the same time, it offers sufficiently fast acquisitions and good dose control.

Another important recent innovation in X-ray imaging is the exploitation of phase effects [4]. Although this is not yet available in clinical practice, the Trieste medical physics group from the SYRMEP beamline of the Elettra synchrotron is carrying out in a pilot study on human patients using synchrotron radiation [5-7]. Among different phase-sensitive techniques, this study uses free space propagation (FSP). This provides edge enhancement of the imaged samples leading to a significant improvement in detail visibility, enabling earlier lesion detection [8]. The FSP implementation is the simplest and was thus considered the most suitable to a first *in vivo* translation on human patients. If the source is sufficiently coherent, optimizing the distance between sample and detector is sufficient to become sensitive to phase effects (alongside absorption).

Due to the demanding requirements that FSP phase contrast imaging (PCI) imposes on the detector resolution, so far the program has been based on mammography screen-film (SF) systems, and the first tests with high-resolution storage phosphor (also termed CR) systems have started only recently. This is suboptimal in many ways, especially as far as films are concerned, as only analogic images are obtained, with limited dynamic range and contrast resolution. An improvement is expected thanks to the transition to storage phosphor systems, however real-time imaging will still not be available, and 3D or quasi-3D approaches consequently impossible. We propose here a possible solution based on the use of a large area CMOS-based X-ray detector developed by Dexela Ltd (a PerkinElmer company).

II. MATERIALS AND METHODS

II.A. Free space propagation phase contrast imaging

FSP PCI is the simplest among phase contrast methods in terms of practical implementation. An object is irradiated by a spatially coherent X-ray beam, and an X-ray detector is placed at a distance

from the object. No additional optical elements are required, as the edge enhancement is due to the interference between the components of the X-ray wave front passing through different parts of the sample, consequently suffering different phase shifts. This can be described by means of near-field (Fresnel) diffraction theory. The intensity distribution at a distance z from the sample is given by:

$$I_z(\vec{r}_\perp) = I_i(\vec{r}_\perp) |T(\vec{r}_\perp) * P_z(\vec{r}_\perp)|^2 \quad (1)$$

where $\vec{r}_\perp = (x, y)$ i.e. the transverse coordinates if we assume that z is the x-ray propagation direction, $I_i(\vec{r}_\perp)$ is the initial intensity of the wave, T is the two-dimensional (2D) transmittance function of the object and $P_z(\vec{r}_\perp)$ is the Fresnel propagator. In the near field region (i.e. for $z < d^2 / \lambda$, where d is the size of the sample and λ is the wavelength), and assuming that the absorption is weak and slowly varying, the intensity measured at the detector plane can be written as:

$$I_z(\vec{r}_\perp) = I_{z=0}(r_\perp) \left[1 - \frac{\lambda z}{2\pi} \bar{\nabla}_\perp^2 \Phi(\vec{r}_\perp) \right] \quad (2)$$

where $\Phi(\vec{r}_\perp)$ is the phase shift caused by the object. The diffraction pattern must then be convolved with the detector point spread function (PSF) [9], which means it becomes increasingly smeared as the detector resolution is decreased. This leads to a reduction of the intensity of the interference fringes, i.e. the phase contrast. Formally a convolution with the (re-scaled) source size should also be performed, but, in the case discussed here (small and distant bending magnet synchrotron source and detector with 75 μm pixel pitch), this is negligible with respect to the detector resolution.

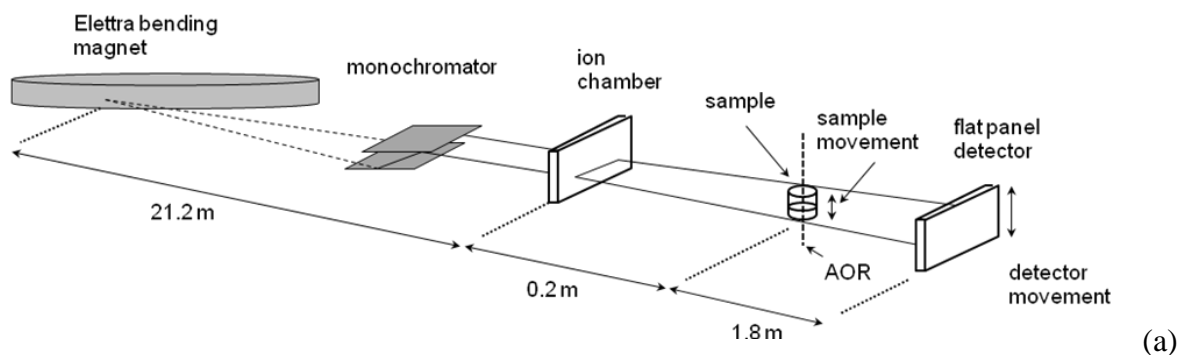
II.B. Prototype detector developed by Dexela Ltd (a PerkinElmer company)

The Dexela 2923 CMOS X-ray detector is based on an APS architecture. In a typical CMOS sensor the photodiode is reset while the charge is accumulated and the charge value is then read out. The APS technology indicates the process of buffering and/or amplification of the signal by a source follower (SF) transistor located in each pixel. This allows better SNR and speeds up the readout process, as the signal is transferred onto a common readout bus as voltage rather than charge. A detailed description of the detector can be found elsewhere [10]. The active area of the detector used for the experiments was 3888 x 3072 pixels, i.e. 29 cm x 23 cm. The detector pixel pitch is 75 μm . The maximum pixel resolution (i.e. no binning) was used, which translates into a maximum readout rate of 26 frames per second. The X-ray performance evaluation of the detector has been tested with

monochromatic synchrotron radiation in the mammographic energy range and reported in [11]. The authors measured the detective quantum efficiency (DQE), which ranges from 0.79 to 0.85 at a frequency of 0.5 lp/mm and at 17 keV and 0.75 to 0.79 at 20 keV. The spatial resolution at 17 keV expressed in 50% MTF is 2.8 lp/mm.

II.C. Experimental conditions

The synchrotron experiments were carried out at the SYRMEP beamline of the Elettra synchrotron radiation facility (Trieste, Italy). Figure 1a shows a schematic drawing of the synchrotron setup. The X-ray beam generated by one of the bending magnets is monochromatized by a double-bounce Si(111) crystal, which enables selecting the required energy with a bandwidth of approximately 0.2% in the range is 8.5-35 keV. Our experiments were performed at 21 keV. Dosimetry measurements were obtained with a ionization chamber placed at about 21 m from the source. The CMOS X-ray detector was mounted on a translation stage at a source-to-detector distance of about 23 m. Tungsten (W) slits were used to limit the beam to a cross-section of 206 mm x 3 mm on the detector surface. During the acquisition, the detector was moved vertically with a speed of 15 mm/s over a range covering the entire sample area. The sample was also simultaneously scanned, at a slightly reduced speed to preserve the angular velocity with respect to the source thus avoiding image distortions.



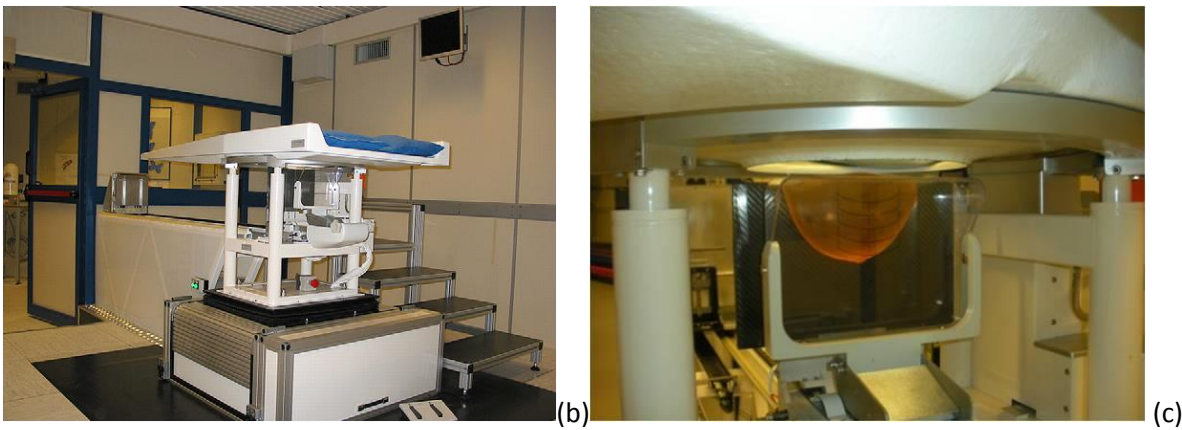


Figure 1 Elettra SYRMEP beam-line experimental setup. Figure adopted from (<http://www.elettra.trieste.it>), modified and mammography facility at SYRMEP beamline: patient support (b) and positioning of the biopsy phantom (c)

In the tomosynthesis experiments at the synchrotron, a rotation stage with an angular resolution of 10^{-3} degrees was used. The biopsy phantom was placed in the patient support (see Figure 1c) used for the *in vivo* procedures. A tomosynthesis scanning method was adopted in which the phantom was rotated (rigidly with the patient bed) about its central position within a non-equiangular range of 40° , while the X-ray source and the detector were kept stationary. A total of 13 projections were collected.

The «standard» tomosynthesis scanning was obtained with the Giotto DBT system, details of which are given in Table 1 The phantom was placed at a distance of 66.6 cm from the source. A set of 13 projections was acquired over a not equiangular range of 40° .

The planar imaging of the ACR phantom was performed with the Senographe Essential (GE) clinical mammography system.

Table 1 Experimental conditions. MGD refers to Mean Glandular Dose and ESAK refers to Entrance Surface Air Kerma.

	Synchrotron imaging		Conventional imaging	
	Planar	tomosynthesis	Planar	Tomosynthesis
energy (mean energy)	21 keV	19 keV	28 kVp (18.4 keV)	27 kVp (19.7 keV)
detector	CMOS APS	CMOS APS	a-Si TFT	a-Se TFT
pixel size	75 μm	75 μm	100 μm	85 μm
anode/filter	NA	NA	Rh/Rh	W/Ag
projections	1	13	1	13
phantom	ACR	Biopsy	Biopsy, ACR	Biopsy
ESAK	2.15 mGy	1.21 mGy		N/A
MGD	0.9 mGy	0.3 mGy (single projection) 4.2 mGy (whole TS scan)	1.1 mGy	0.2 mGy (single projection) 2.7 mGy (whole TS scan)

All images were gain and offset corrected to remove pixel-to-pixel variations and non-uniformities in the irradiation profile. The tomosynthesis slices were reconstructed with an iterative algorithm provided by Dexela Ltd, based on the Separable Paraboloidal Surrogates (SPS) algorithm. More details on the reconstruction method can be found in [12].

For planar imaging we used a 4.5 cm thick ACR mammography accreditation phantom (Figure 2a), which contains test objects placed in a wax block. The details included in the wax layer simulate typical breast pathologies: fibres, microcalcifications and tumour masses.

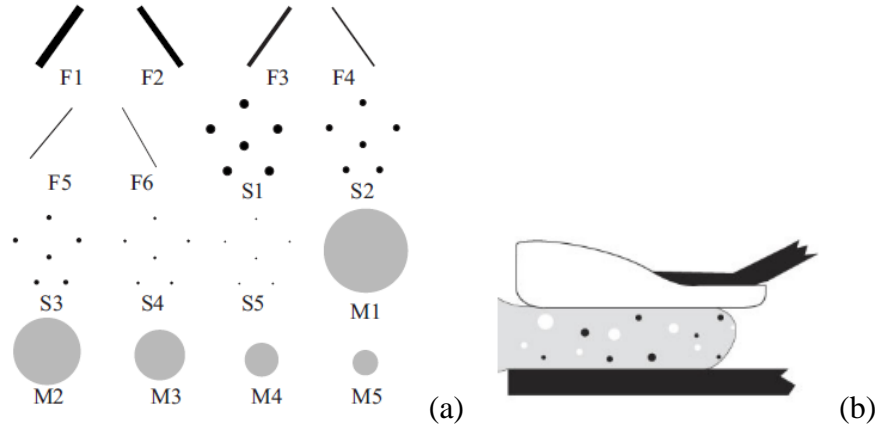


Figure 2 American College of Radiology (ACR) accreditation phantom (a) containing six fibres (F1 to F6) with the thickness varying between 1.56 mm and 0.4 mm, five groups of microcalcification specks (S1 to S5) with the diameter between 0.54 mm (S1) and 0.16 mm (S5) and five tumour-like masses (M1 to M5) with the diameter of between 2 mm and 0.16 mm. (b) Stereotactic biopsy phantom placed between compression pads.

A Stereotactic Needle Biopsy Phantom (Figure 2b) was used for both planar and tomosynthesis imaging. The phantom is a standard tool for quality assurance in stereotactic systems. The phantom is shaped as to represent a partially compressed breast with a standard thickness of 4.5 cm. A number of randomly placed solid masses in the range of 3 to 6 mm simulate tumour masses. Two calcifications clusters are positioned in a middle plane of the phantom. The diameters of the calcifications range from 300 μm to 350 μm .

The mean glandular dose (MGD) delivered to the sample was calculated based on the European [13] and IAEA [14] protocols for Dosimetry in conventional mammography. According to [15], the MGD can be calculated as:

$$MGD = K_a gcs \quad (6)$$

where K_a corresponds to the air kerma measured at the surface of the breast, g and c are the conversion factors that correspond to the glandularity level of the breast (in this case g corresponds to 50% glandularity of the breast while c allows for different levels of glandularity); s is the

conversion factor used to account for different x-ray spectra. In this study, the normalized glandular dose coefficients for monochromatic x-rays were taken from [16].

The above definition of MGD can be extended to a tomosynthesis geometry by adding two further correction factors: t-factors and T-factors [17]. The t-factors correspond to a single projection at a given angle θ and depend upon the x-ray spectra, breast sizes and glandularities, while the T-factors take into account the complete tomosynthesis scan and depend on the choice of projection angles and weights per projection. These factors have primarily a geometrical origin for both the clinical and the synchrotron setups. According to [17], the correction factor T for an angular range of -20° to 20° and a breast thickness of 40 mm would be 0.973, giving a difference of 2.7 % on the MGD. This difference would thus be even smaller for the angular range used in this work, and was therefore neglected. It should also be noted that the clinical tomosynthesis was performed at higher x-ray tube voltage than the usual clinical practice (and delivering higher dose to the phantom) to match the synchrotron values.

The quantitative analysis of the images was based on the contrast-to-noise ratio (CNR), a commonly used parameter for the assessment of the image quality. In conventional absorption-based imaging, the CNR_{ABS} is calculated as the difference between the intensity value of a feature $I_{feature}$ and the intensity value of the background I_{bg} , divided by the standard deviation of the intensity values of the background σ_{bg} : $CNR_{ABS} = (I_{feature} - I_{bg}) / \sigma_{bg}$. Phase contrast images are characterized by intense positive and negative peaks; Hence, the contrast is redefined on the basis of the difference between maximum and minimum peak intensities ($C = (I_{max} - I_{min}) / I_{bg}$) [18]; the CNR is consequently redefined as:

$$CNR_{PC} = \frac{I_{max} - I_{min}}{\sigma_{bg}} \quad (7)$$

III. RESULTS AND DISCUSSIONS

III.A. Planar imaging

Figure 3 shows a comparison between conventional and synchrotron radiation planar images of different regions of interest (ROIs) within the ACR phantom. Since the acceptable clinical level of MGD delivered in two projections to a breast equivalent thickness of 4.5 cm is 2 mGy [19], we kept the MGD close to 1 mGy per image in both synchrotron and clinical experiments. The specks with a diameter equal and larger than 320 μm were easily detectable in both conventional and synchrotron

images. The specks with a diameter of 160 μm were detectable only in the synchrotron images. The lower limit of the thickness of fibres for the conventional system was 750 μm , while fibre thicknesses down to 400 μm were detected in the synchrotron images. Phase contrast effects are visible at the edges of the fibres as dark and bright fringes. Significant advantages were observed also on the imaging of the masses, as details with a diameter of 160 μm were detectable in synchrotron images, while the conventional system was limited to masses with a diameter of 500 μm .

Figure 4 shows a planar image of a region of about 600 x 1000 pixels of the biopsy breast phantom (corresponding to approximately half the image). A superior contrast of the tumour masses and calcifications can be observed in the synchrotron image compared to the conventional one. In the synchrotron images, phase contrast effects are visible at the boundaries of the tumour-like masses as dark and bright fringes on the immediate inside and outside of the mass, respectively.

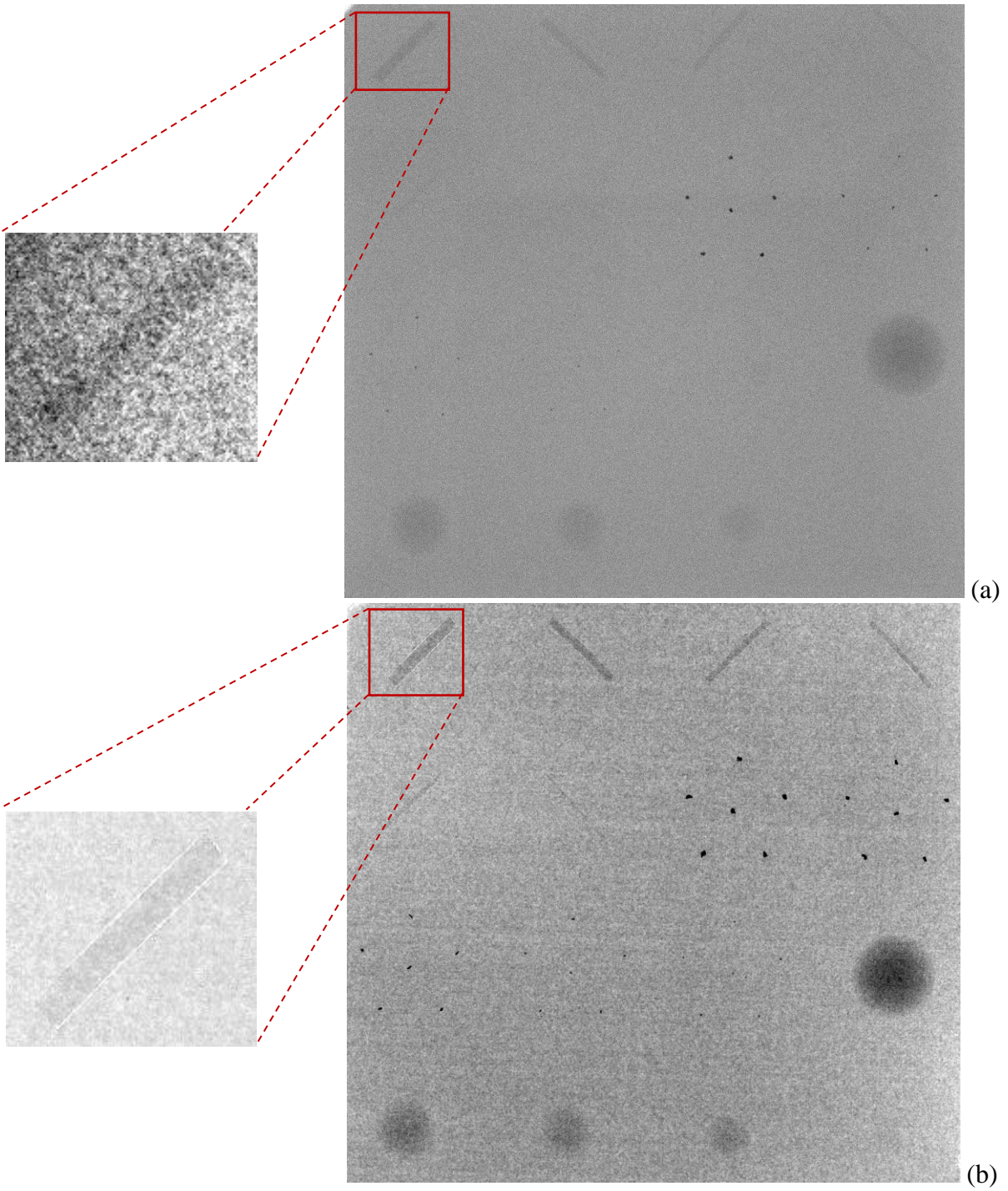


Figure 3 Images of an ACR phantom with a selected ROI (left) obtained with a) a clinical system and b) using synchrotron radiation

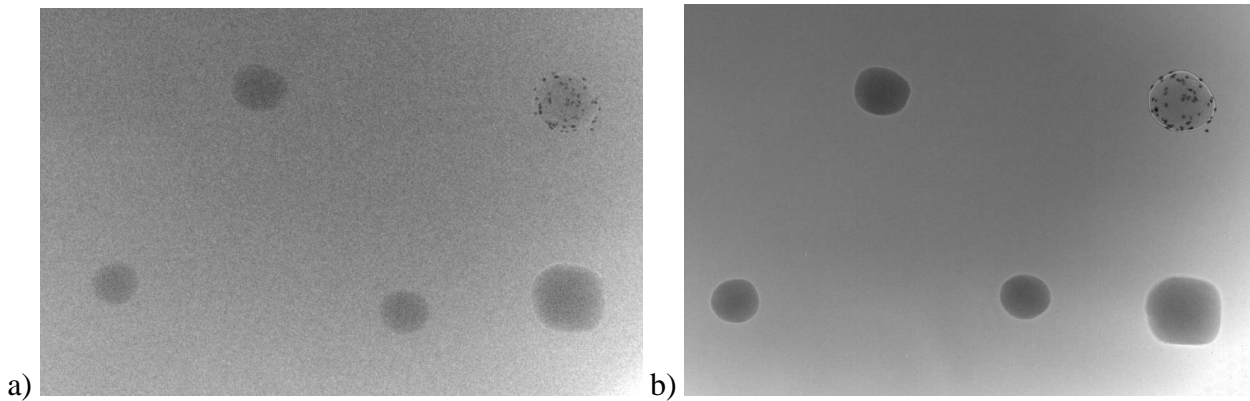


Figure 4 Single projection image of an ROI in the biopsy phantom obtained with (a) clinical tomosynthesis system and (b) synchrotron radiation. The gradient visible in both images (e.g. bottom right corner) has probably been caused by not-ideal gain and offset corrections.

III.B. Digital Tomosynthesis of the biopsy breast phantom

The MGD delivered to the sample during one tomosynthesis projection at the synchrotron was estimated to be 0.3 mGy, while it was 0.2 mGy for the conventional tomosynthesis image. The MGD of the entire tomosynthesis scan was therefore 4.2 mGy and 2.7 mGy for the synchrotron and conventional acquisitions, respectively. For comparison, in DBT a typical MGD for a 4.5 cm thick phantom ranges from 1.9 mGy to 2.1 mGy, depending on the system [20]. Three reconstructed slices are presented in Figure 5, which shows images obtained with both the clinical system and synchrotron radiation. The reconstruction planes are 0.5 mm thick, and cover the entire phantom area (i.e. 20 cm x 15 cm). Ten iteration steps were used in the reconstruction. Out of plane objects cause blurring artefacts, while the edges of the objects in the plane of focus are crisp and exhibit phase contrast edge enhancement.

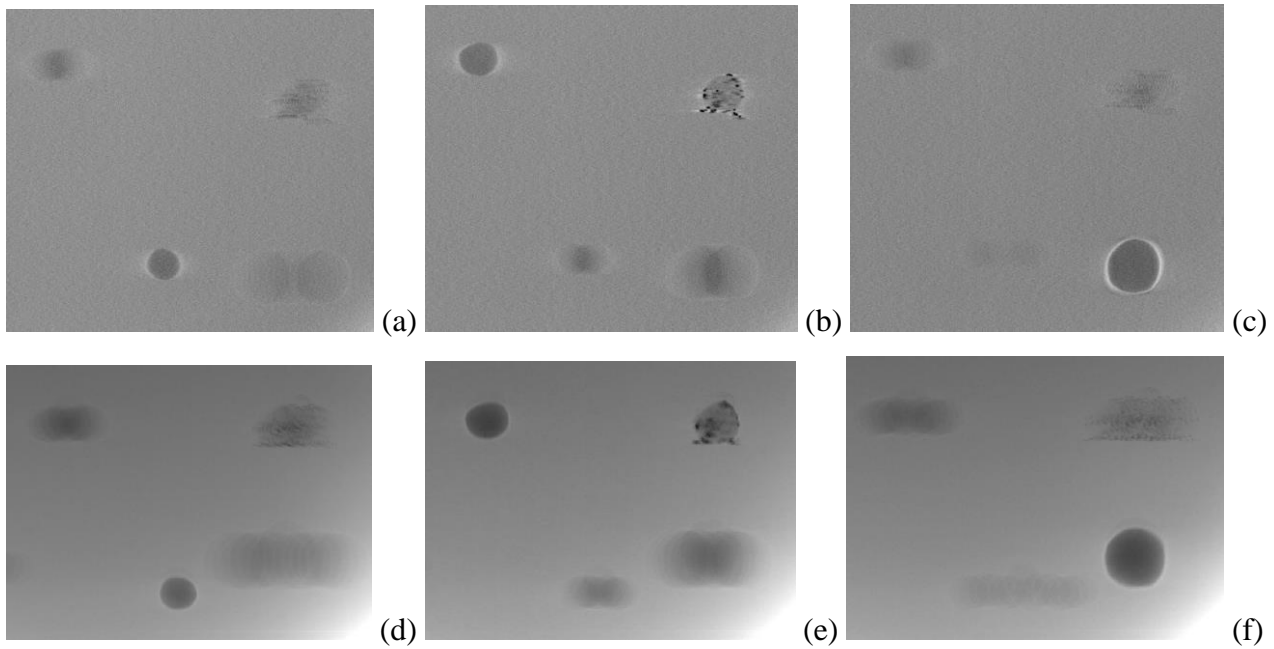


Figure 5 Selected reconstructions of the biopsy phantom obtained with the clinical tomosynthesis system (a-c) and using synchrotron radiation (d-f). Different features are in focus when slicing through the reconstructed volume from left to right. The objects that are not in the plane of focus appear as multiple replicas causing blurring artefacts.

Figure 6 shows a comparison between the signal obtained with the clinical system and synchrotron radiation for a single projection ROI at angle 0° containing a tumour-like mass. Although the phase contrast signal is weak (due to the excessively large pixel size washing out the phase contrast fringes), it can be still clearly observed at the boundaries of the detail in the synchrotron images (see arrows in Figure 6). The image contrast is two times larger in the synchrotron images than in those obtained with a clinical system (see Figure 8). Likewise, a significant increase in the CNR can be seen for the synchrotron images. It should be noted however that the higher contrast in the phase contrast images might be partially caused by the reconstruction algorithm, which was primarily designed for the absorption-based images.

Figure 7 shows an ROI of the reconstructed tomosynthesis image of the same tumour-like object. While the images obtained with synchrotron radiation preserve the phase contrast signal, this is missing from the image taken with the clinical system (see the vertical profile plot in Figure 7c). The bright fringes visible in the clinical image are not due to phase effects as they only appear on the sides of the objects and not all around it. These artefacts are due to the air gaps between the details and the phantom gel, and are intensified by the reconstruction algorithm. If these are ignored, both image contrast and CNR (shown in Figure 10) are superior for the images obtained with the synchrotron radiation compared to those taken with a clinical system.

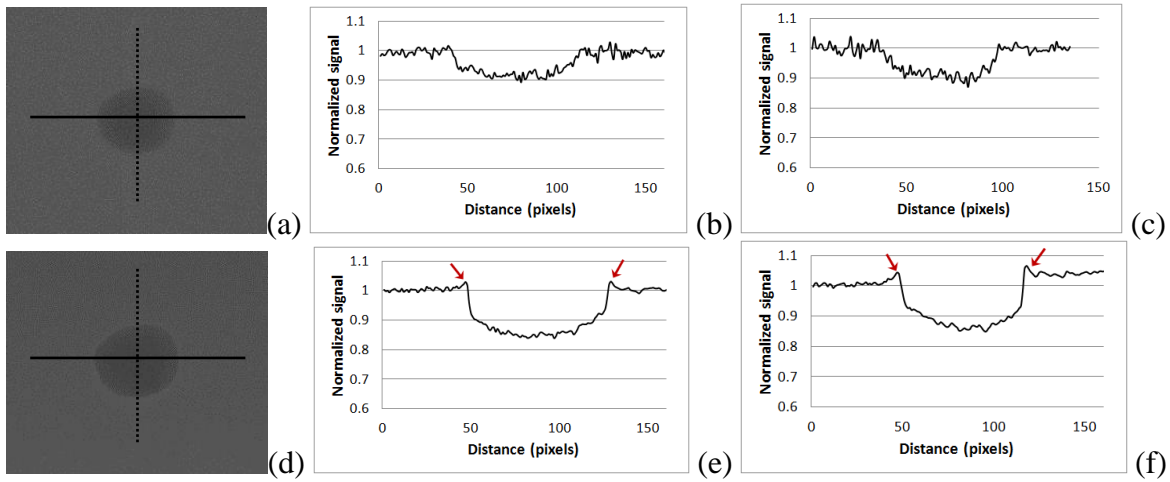


Figure 6 Single projections at 0° (a, d) and corresponding horizontal (b, e) and vertical (c, f) profile plots obtained with a conventional TS system (a, b, c) and with synchrotron radiation (d, e, f). The arrows show the signal build-up due to the phase contrast effects.

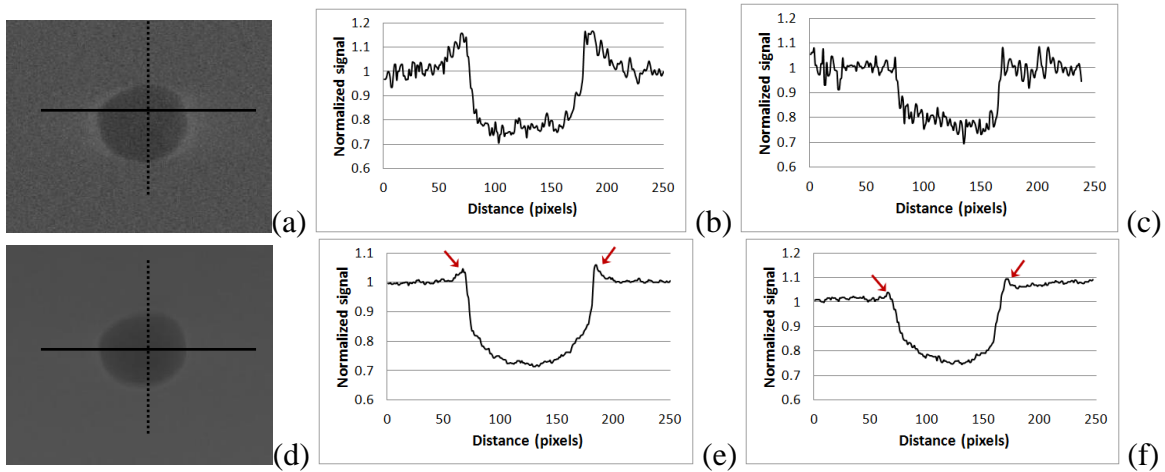


Figure 7 Reconstructions (a, d) and corresponding horizontal (b, e) and vertical (c, f) profile plots obtained with a conventional TS system (a, b, c) and with synchrotron radiation (d, e, f). The build-up of the signal indicated by the arrows is only present in the synchrotron images and is caused by the phase contrast effects.

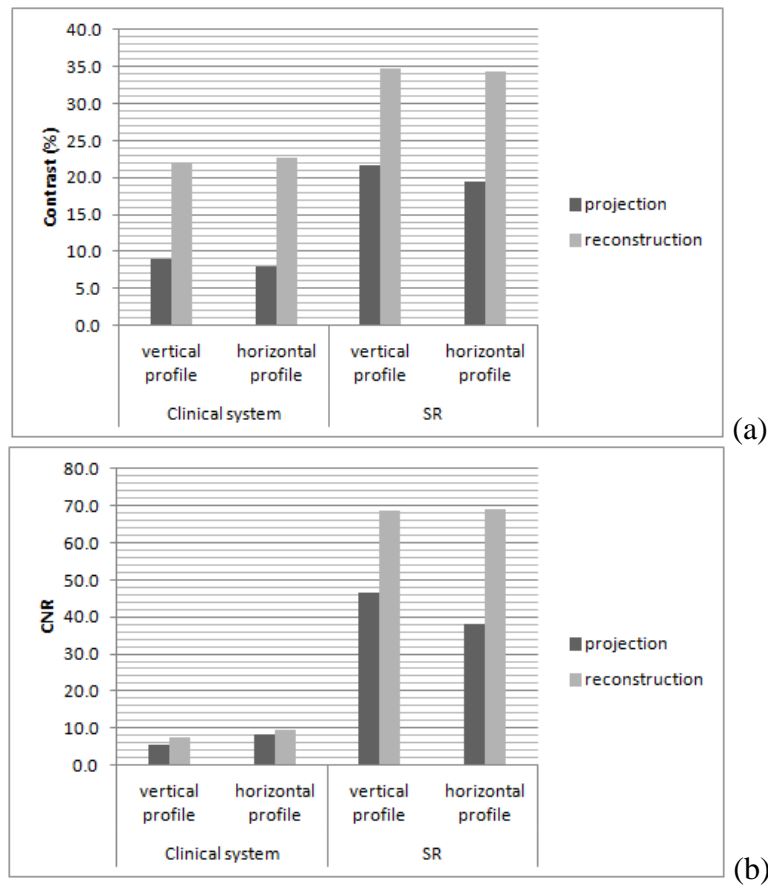


Figure 8 Contrast and CNR calculated for the clinical and synchrotron projection and reconstructed image from Figure 6 and Figure 7.

IV. CONCLUSIONS

The purpose of this study was to test the imaging performance of a novel CMOS APS X-ray detector at the only *in vivo* mammography synchrotron beamline, and compare the obtained images with those acquired with a clinical system. A considerably higher image contrast was obtained at the synchrotron for both planar and tomosynthesis images with respect to conventional mammograms and reconstructed tomosynthesis slices. The reason for this is twofold. First, the image contrast of the synchrotron images is enhanced thanks to the superior characteristics of the synchrotron beam (e.g. monochromaticity), as well as scatter reduction due to air gap and possibly tight beam collimation. Secondly, and possibly most importantly, image improvement originates from the edge enhancement induced by FSP phase contrast fringes. Despite the blurring effect due to a relatively large pixel size of 75 μm , these were still clearly appreciable in practically all synchrotron images. This is promising both in terms of replacing the current screen-film systems and storage phosphor systems used by the *in vivo* study in Trieste, and for future developments regarding the translation of phase contrast methods into clinical practice. Clearly, should detectors with comparable performance and smaller pixel size become commercially available in the near future, even stronger image enhancements due to phase effects would be expected.

ACKNOWLEDGEMENTS

M. B. Szafraniec was partially funded by an EPSRC-GB doctoral training allowance, A. Olivo is supported by the UK Engineering and Physical Sciences Research Council (grants EP/G004250/1 and I021884/1). The detector was supported by Dexela Ltd. (a PerkinElmer company).

REFERENCES

- [1] Izadi MH, Karim KS. Noise analysis of a CMOS active pixel sensor for tomographic mammography. *Fifth International Workshop on System-on-Chip for Real-Time Applications, Proceedings*. 2005;167-71.
- [2] Taghibakhsh F, Karim KS. High resolution amplified pixel sensor architectures for large area digital mammography tomosynthesis - art. no. 69133R. *Medical Imaging 2008: Physics of Medical Imaging, Pts 1-3*. 2008;6913:R9133-R.
- [3] Dobbins JT, Godfrey DJ. Digital x-ray tomosynthesis: current state of the art and clinical potential. *Physics in Medicine and Biology*. 2003;48:R65-R106.
- [4] Bravin A, Coan P, Suortti P. X-ray phase-contrast imaging: from pre-clinical applications towards clinics. *Phys Med Biol*. 2013;58:R1-35.
- [5] Arfelli F, Abrami A, Bregant P, Chenda V, Cova MA, de Guarrini F, et al. Synchrotron radiation mammography: Clinical experimentation. *Synchrotron Radiation Instrumentation, Pts 1 and 2*. 2007;879:1895-8.
- [6] Castelli E, Arfelli F, Dreossi D, Longo R, Rokvic T, Cova MA, et al. Clinical mammography at the SYRMEP beam line. *Nuclear Instruments & Methods in Physics Research Section a-Accelerators Spectrometers Detectors and Associated Equipment*. 2007;572:237-40.
- [7] Dreossi D, Abrami A, Arfelli F, Bregant R, Casarin K, Chenda V, et al. The mammography project at the SYRMEP beamline. *European Journal of Radiology*. 2008;68:S58-S62.
- [8] Arfelli F, Assante M, Bonvicini V, Bravin A, Cantatore G, Castelli E, et al. Low-dose phase contrast x-ray medical imaging. *Phys Med Biol*. 1998;43:2845-52.
- [9] Olivo A, Speller R. Experimental validation of a simple model capable of predicting the phase contrast imaging capabilities of any x-ray imaging system. *Physics in Medicine and Biology*. 2006;51:3015-30.
- [10] Konstantinidis AC, Szafraniec MB, Speller RD, Olivo A. The Dexela 2923 CMOS X-ray detector: A flat panel detector based on CMOS active pixel sensors for medical imaging applications. *Nuclear Instruments & Methods in Physics Research Section a-Accelerators Spectrometers Detectors and Associated Equipment*. 2012;689:12-21.
- [11] Konstantinidis AC, Szafraniec MB, Rigon L, Tromba G, Dreossi D, Sodini N, et al. X-ray Performance Evaluation of the Dexela CMOS APS X-ray Detector Using Monochromatic Synchrotron Radiation in the Mammographic Energy Range. *Nuclear Science, IEEE Transactions on*. 2013;60:3969-80.
- [12] Szafraniec MB, Millard TP, Ignatyev K, Speller RD, Olivo A. Proof-of-concept demonstration of edge-illumination x-ray phase contrast imaging combined with tomosynthesis. *Phys Med Biol*. 2014;59:N1-10.
- [13] EC. European guidelines for quality assurance in breast cancer screening and diagnosis (fourth edn.). European Commission, Luxembourg, Office for Official Publications of the European Communities; 2006.
- [14] IAEA. Dosimetry in diagnostic radiology: an international code of practice Technical Reports Series no 457 (Vienna: IAEA) Vienna: IAEA: International Atomic Energy Agency (IAEA); <http://www-pub.iaea.org/>

MTCD/publications/PDF/TRS457_web.pdf; 2006.

[15] Dance DR, Young KC, van Engen RE. Further factors for the estimation of mean glandular dose using the United Kingdom, European and IAEA breast dosimetry protocols. *Physics in Medicine and Biology*. 2009;54:4361-72.

[16] Boone JM. Glandular breast dose for monoenergetic and high-energy X-ray beams: Monte Carlo assessment. *Radiology*. 1999;213:23-37.

[17] Dance DR, Young KC, van Engen RE. Estimation of mean glandular dose for breast tomosynthesis: factors for use with the UK, European and IAEA breast dosimetry protocols. *Physics in Medicine and Biology*. 2011;56:453-71.

[18] Pagot E, Fiedler S, Cloetens P, Bravin A, Coan P, Fezzaa K, et al. Quantitative comparison between two phase contrast techniques: diffraction enhanced imaging and phase propagation imaging. *Phys Med Biol*. 2005;50:709-24.

[19] Young K, Strowig M, Mills J. Modelling of the effect of organ motion combined with field parameters on the received dose to a target region. *Radiother Oncol*. 2005;76:S156-S7.

[20] Dance D, Strudley C, Young K, Oduko J, Whelehan P, Mungutroy EHL. Comparison of Breast Doses for Digital Tomosynthesis Estimated from Patient Exposures and Using PMMA Breast Phantoms. In: Maidment AA, Bakic P, Gavenonis S, editors. *Breast Imaging*: Springer Berlin Heidelberg; 2012. p. 316-21.